RMetS
Royal Meteorological Society

Probability of intense precipitation from polarimetric GNSS radio occultation observations

E. Cardellach,[a]* R. Padullés,[a] S. Tomás,[a] F. J. Turk,[b] C. O. Ao[b] and M. de la Torre-Juárez[b]

[a]*Institute of Space Sciences (ICE-CSIC/IEEC), Barcelona, Spain*
[b]*Jet Propulsion Laboratory, California Institute of Technology, Pasadena, USA*

*Correspondence to: E. Cardellach, ICE-CSIC/IEEC, Campus UAB, C/ Can Magrans S/N, 08193 Cerdanyola del Vallès, Barcelona, Spain. E-mail: estel@ice.csic.es

There is currently a gap in satellite observations of the moisture structure during heavy precipitation conditions, since infrared and microwave sounders cannot sense water-vapour structure near the surface in the presence of intense precipitation. Conversely, Global Navigation Satellite System (GNSS) radio occultations (RO) can profile the moisture structure with high precision and vertical resolution, but cannot indicate the presence of precipitation directly. Polarimetric RO (PRO) measurements have been proposed as a method to characterize heavy rain in GNSS RO, by measuring the polarimetric differential phase delay induced by large size hydrometeors. Previous studies have shown that the PRO polarimetric phase shift is sensitive to the path-integrated rain rate under intense precipitation scenarios, but there is no current method to invert PRO measurements into quantitative estimates of the path-averaged rain rate. In this manuscript, a probabilistic inversion approach to the GNSS PRO observables is proposed, where the GPM precipitation products are used for the construction of an *a priori* look-up table (LUT) database. The performance of the LUTs is assessed for use in the inversion of satellite-based GNSS PRO observations, based on synthetically generated PRO data of actual events, which correspond to co-locations between GNSS RO profiles and the TRMM observations. The synthetic data include end-to-end propagation effects of the polarimetric observables and a simple separation algorithm to isolate the hydrometeor component of the observation. The assessment results in agreement better than $\pm 1\,\mathrm{mm\,h^{-1}}$ between the reference LUT and the actual rain statistics of the synthetic data, proving the suitability of the GPM-based probabilistic inversion tool. These findings indicate that the GNSS PRO products are capable of extending the current GNSS RO ones by associating indications of rain-rate probabilities at different altitudes, at ∼250 m vertical resolution and under intense precipitation scenarios with the standard vertical thermodynamic profiles.

Key Words: global navigation satellite signals (GNSS); radio occultations (RO); polarimetric radio occultations (PRO); remote sensing of precipitation; thermodynamic profiles

Received 05 May 2017; Revised 31 July 2017; Accepted 15 September 2017; Published online in Wiley Online Library

1. Introduction

Recent national and international assessments (Hartmann *et al.*, 2013; Kunkel *et al.*, 2013) have indicated a global trend towards more frequent heavy precipitation events, representing potentially severe impacts to human life and property. However, our incomplete understanding of the physical processes that drive extreme precipitation hinders the ability of the current models to resolve these events accurately. Among the multiple interconnected processes influencing the moisture structure and precipitation state, fundamental questions related to the origin, concentration and influence of water vapour remain unanswered (e.g. Masunaga, 2014; Westra *et al.*, 2014; Schiro *et al.*, 2016). The driver of atmospheric circulation is convection, which by itself can modify the moisture distribution through vertical transport and detrainment and, in the sub-cloud layer, through the evaporation of precipitation and clouds. Multiple theories regarding the large-scale (∼10–1000 km) processes that result in such heavy precipitation have been postulated, with recent evidence pointing to control by free-tropospheric moisture (Derbyshire *et al.*, 2004; Schiro *et al.*, 2016). Without an improved understanding and representation of the processes that link tropospheric water vapour and heavy precipitation, the disparities between model representations of heavy precipitation and observations are likely to persist (e.g. Dai, 2006).

From an observational standpoint, hyperspectral infrared sounders such as the Advanced Infrared Sounder (AIRS) aboard the NASA *Aqua* satellite can profile the lower tropospheric

temperature and humidity structure within the cloud-free environment surrounding cloudy areas, but the quality and quantity of valid data degrade very rapidly within cloud cover (Susskind *et al.*, 2003). Passive microwave humidity sounders that operate in the 183 GHz water-vapour absorption complex, such as the Advanced Technology Microwave Sounder (ATMS) aboard the *Suomi National Polar-orbiting Partnership* (*Suomi-NPP*) operational platform, can provide profiles within cloud cover to a somewhat larger extent, but do not sense directly within the boundary layer inside heavy convection. Space-based precipitation radar systems include the Precipitation Radar (PR) and Dual-Frequency Precipitation Radar (DPR) aboard the *Tropical Rainfall Measuring Mission* (*TRMM*, 1997–2014: Kummerow *et al.*, 2015) and the Global Precipitation Measurement (GPM, 2014–current: Hou *et al.*, 2014; Skofronick-Jackson *et al.*, 2016) core observatory, respectively. These radars intentionally operate at attenuating frequencies (Ku/Ka band or 13.6/35.5 GHz for DPR; only Ku band for PR), where path attenuation can be used as a constraint to improve the estimation of the condensed water profile and the associated surface rainfall rate. While the radar backscatter represents the net effects of scattering and attenuation due to water vapour and rainfall, the two cannot be readily separated to determine the water-vapour profile internal to the precipitation core. There is also evidence highlighting the degradation of retrievals of intense convective precipitation owing to multiple scattering (Battaglia *et al.*, 2015, 2016) and non-uniform beam-filling issues (Durden and Tanelli, 2008). The issue is more acute over land surfaces, where the path attenuation technique has problems. This yields larger uncertainties in the precipitation retrievals, also affected by highly variable radar surface backscatter (Seto and Iguchi, 2007). In summary, neither IR instruments like AIRS nor GPM are particularly suited for observations of the joint structure of water vapour internal to heavily precipitating clouds. The very same factors that influence or affect one measurement (water vapour or precipitation) are difficult to extract from, or indirectly influence, the observation of the other.

Radio occultation (RO) techniques take advantage of radio signals transmitted by the expanding networks of Global Navigation Satellite Systems (GNSS), notably the US Global Positioning System (GPS). The six-satellite *COSMIC/FORMOSAT-3* constellation (e.g. Anthes *et al.*, 2008) and the future *COSMIC-2/FORMOSAT-7* (e.g. Lee *et al.*, 2013) follow-on provide a wealth of data for weather and climate applications, providing a relatively inexpensive approach for sounding the global atmosphere with high precision, accuracy and vertical resolution, seamlessly through precipitation and across land–ocean boundaries. Several studies within the past decade have demonstrated the positive impact that results when RO is assimilated into numerical weather prediction models by operational forecast agencies (e.g. Cardinali and Healy, 2014).

The material in this article involves a newly proposed measurement concept, where GNSS RO measurements are taken at two orthogonal polarizations to exploit the potential capabilities of polarimetric RO (PRO) for jointly observing and quantifying atmospheric thermodynamics and rain profiles within heavy precipitation events (Cardellach *et al.*, 2015). These polarimetric RO measurements are predicated on the fact that, in the L band (1.5 GHz, the typical GNSS transmit frequency), the effect of clouds and precipitation on the received signal magnitude is negligible, but since GNSS receivers provide inherently high precision phase measurements they can track differential propagation phase changes very accurately. Since precipitation-sized hydrometeors are typically aspherically shaped, the differential phase of the received signal is modified during tangential propagation through clouds associated with heavy precipitation. In the case of PRO, propagation through liquid precipitation or large crystalline ice (Vivekanandan *et al.*, 1994) will induce a cross-polarized component (Padullés *et al.*, 2016a). The measurement of differential propagation phase shifts has been studied in detail by the ground-based weather radar community (Bringi *et al.*, 1990) and is now an integral part of the USA nationwide Next-Generation Radar (NEXRAD) radar system (e.g. Cunha *et al.*, 2013). If this differential measurement concept is demonstrated for space-based observations, PRO may introduce new applications of GNSS RO observations by profiling high vertical resolution (∼250 m) coincident thermodynamic conditions within clouds associated with regions of heavy precipitation, subject of course to the viewing conditions associated with GNSS RO measurements (i.e. relatively coarse ∼150 km horizontal structure but fine vertical structure). While individual convective clouds are typically associated with scales up to 100 times finer than this, large-scale precipitation systems in the Tropics are not far from this scale. Based on a multi-year study of TRMM data, Liu *et al.* (2008) determined that precipitation features greater than 10 000 km^2 contribute more than 50% of the total precipitation over the tropical oceans and 70% over the southeastern USA. Similar statistics were determined independently by Nesbitt *et al.* (2006) in a separate TRMM-based study.

The combined information in GNSS PRO high vertical resolution (∼250 m) rain profiles and coincident thermodynamic conditions within regions of heavy precipitation also provides other potential benefits. For example, knowledge of the presence of precipitation is useful to improve and evaluate the cloud microphysical parametrizations used in numerical weather prediction (NWP) forecast models, where the local environment affects the transition of condensed water from cloud to rain. Since heavy precipitation is often associated with strong vertical air motion, these observations may lead to better understanding of cloud processes and thermodynamic conditions within convective cloud structures. The unique value of the GNSS PRO measurements in the context of other current and planned space-based missions is the capability simultaneously and directly to measure the vertical structure of water vapour and yield an indication of heavy precipitation at each level.

An earlier study by the authors (Cardellach *et al.*, 2015) discussed the design and expected hydrometeor sensitivity of the Radio Occultations and Heavy Precipitation (ROHP) PRO experiment, which is included aboard the Spanish Earth observation *PAZ* satellite, currently planned for launch in 2017. The ROHP–PAZ experiment is based on a modified, JPL-designed, Integrated GPS Occultation Receiver (IGOR+) GNSS receiver. The main payload of *PAZ* is an X-band synthetic aperture radar (SAR), decoupled from and not used by the ROHP–PAZ experiment. The GNSS PRO technique was confirmed further in an experimental field campaign from a mountain top (Padullés *et al.*, 2016a). A preliminary data-processing technique to resolve precipitation structures from GNSS PRO was introduced by Padullés *et al.* (2016b), but they showed that it would work only under certain limited conditions. The difficulty in resolving the structures lies in the fact that the PRO measurement provides only the total path propagation differential phase (the equivalent of phi-DP in the case of a ground-based polarimetric radar, but in forward scattering rather than backscattering). Unlike a radar that provides range sampling, it is not possible to invert the PRO measurements directly into specific rain rates along the satellite-to-satellite rays. Nevertheless, the considerable number of satellite-to-satellite coincidences between the large number of existing GNSS RO and overpasses of either GPM or TRMM radar can be exploited to build a large number of *a priori* observations of the joint structure of water vapour and precipitation. Given a sufficiently large and representative *a priori* dataset of these observations, the path-averaged rain rate and its uncertainty can be estimated in a Bayesian sense from the PRO observations alone. This methodology is similar to the idea behind Bayesian methods applied to passive microwave retrievals of precipitation, which uses an extensive *a priori* dataset of precipitation profile information from the DPR or PR to invert the radiometer brightness temperatures (Kummerow *et al.*, 2015).

In this study, we propose a probabilistic inversion retrieval of the spaceborne GNSS PRO data. The approach is based upon look-up tables (LUTs) that relate the propagation total polarimetric differential phase to realistic rain conditions. The LUTs will act as reference statistical tools to determine the likelihood of each ray in a GNSS PRO sounding having crossed precipitation cells of a certain intensity. The generation of the reference LUT is presented in section 3, based on an extensive artificial co-location between RO ray trajectories and GPM DPR precipitation profiles, where only the hydrometeor component of the polarimetric phase shift has been considered. The validation of such a probabilistic retrieval approach cannot be performed using individual cases, but rather a new set of events, to check that they indeed follow the retrieved probability distribution. This probabilistic validation exercise is carried out in section 4 using actual GNSS RO events co-located with actual TRMM 3D precipitation data. Unlike the generation of the reference LUT, the validation set is based on synthetic data resulting from a more complete end-to-end (E2E) simulation. These data sets now include the multiple factors that influence the RO polarimetric propagation from the transmitter to the receiver (transmitter polarimetric impurities, ionospheric effects before and after the precipitation cells and receiver instrumental issues). An algorithm to isolate the hydrometeor component of the observables from other effects, summarized in section 2, is applied to the end-to-end data, so finally the LUT inversion scheme can be tested. The study concludes with a set of illustrative cases in section 5, to show how the method would be applied to actual GNSS PRO data and the geophysical products it would generate.

2. The GNSS PRO sounding concept

A radio occultation is an atmospheric sensing technique created for planetary exploration (e.g. Phinney and Anderson, 1968). It measures the bending suffered by electromagnetic signals when crossing the planet's atmosphere, on their way from an opportunistic transmitter to a dedicated receiver. The bending is due to vertical gradients in the refractive index of the atmosphere, which acts as a lens. The principle of measurement, therefore, is inversion from the bending of the signals to the vertical profile of the refractive index $n(h)$ (or refractivity, defined as $N(h) = (n-1) \times 10^6$). On Earth, the technique uses opportunistic signals transmitted by the navigation systems (Global Navigation Satellite Systems (GNSS), such as the Global Positioning System (GPS)) and the receivers, which tend to be aboard Low Earth Orbiters (LEO), although airborne GNSS RO are also possible (e.g. Healy *et al.*, 2002; Xie *et al.*, 2008). GNSS signals are emitted in the L band (~0.2 m wavelength) in circular polarization (right-hand circular, RHCP). This electromagnetic band was chosen to enable all-weather penetration (including thick clouds and intense precipitation), while circular polarization was chosen to overcome polarization mismatch under any arbitrary geometry. Further details about GNSS signals and applications can be found in e.g. Spilker et al. (1996), Jin et al. (2014) and Teunissen and Montenbruck (2017).

In a standard GNSS RO receiving system, a dedicated RHCP antenna is placed at the front or rear (with respect to the movement) of a satellite, pointing towards the limb of the Earth. The basic difference between a standard and a polarimetric GNSS RO is that the circularly polarized receiving antenna is replaced by a 2-linear polarized one in the GNSS PRO concept. Each port of the antenna (H for horizontally polarized and V for vertically polarized) is connected to one port of the dedicated receiver, which treats both entries synchronously (as set up in the ROHP–PAZ experiment).

The geometry of both GNSS RO and GNSS PRO is identical (see Figure 1). In a setting RO, the receiver and transmitter are initially high in the sky and gradually settle down below the horizon, with the Earth blocking its line of sight (occulting each other). The radio link crosses many layers of the atmosphere,

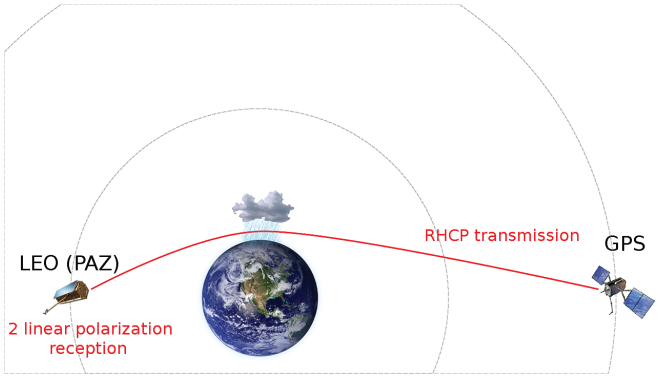

Figure 1. Sketch of the GNSS PRO geometry (not scaled). The signals transmitted by a satellite of the GNSS constellation are acquired by a Low Earth Orbiter in occulting geometry, when the Earth blocks their straight line of sight. The atmosphere, by means of its vertical gradients, acts like a lens and bends the radio-link trajectory (or ray). The bending is measured precisely by GNSS RO standard techniques (also from GNSS PRO acquisition systems). The geometry of GNSS RO and GNSS PRO is the same, as the only difference between both techniques is the polarization capabilities of the receiving system aboard the LEO. *PAZ* is the GNSS PRO proof-of-concept mission (launch planned 4th quarter in 2017).

from outer space down to the tangent point, which is the location of the ray closest to the surface and with propagation direction parallel to it. The altitude of the tangent point will be denoted h_t hereafter. The GNSS receiver indirectly measures the bending of the radio link and this can be inverted into vertical profiles of atmospheric refractivity (e.g. Kursinski *et al.*, 1997). The resulting refractivity measurement at the troposphere has an approximate resolution of 100–200 m in the vertical direction and of the order of ~100 km along the ray direction, centred at the tangent point.

In the ROHP–PAZ experiment, the polarimetric radio occultation observable is defined as the phase shift between the two linear polarization channels of the receiving system. When expressed in vertical and horizontal polarizations, hydrometeors induce a shift that relates to the different delay suffered by the signal crossing the droplets along its longer horizontal axis with respect to the delay suffered when it crosses its shorter vertical axis. Only intense rain induces this effect at detectable levels (Cardellach *et al.*, 2015), as large droplets are required for the air friction to flatten them. This polarimetric phase shift, here also called polarimetric phase delay and usually given in units of length (e.g. mm of GPS L1 wavelength λ_{mm}, i.e. $\Phi_{mm} = \lambda_{mm}\Phi_{rad}/(2\pi)$), is the cumulated phase shift given by the forward-scattering specific differential phase K_{dp} at each point along the GNSS ray, which in turn depends on the drop size distribution $N(D)$ and forward-scattering amplitudes f_H and f_V corresponding to the scattering of H and V polarized signals off a single D-sized drop (Cardellach *et al.*, 2015):

$$\begin{aligned}\Delta\Phi_{hyd} &= \int_L K_{dp}(l)\,dl \\ &= \frac{\lambda^2}{2\pi}\int_L \left[\int \Re\{f_H(D) - f_V(D)\}N(D)\,dD\right] dl, \end{aligned} \quad (1)$$

where $\Re$ stands for the real part, $N(D)$ denotes the number of drops in a cubic metre per drop-size interval in mm and D is the equivolumetric drop diameter, also in mm. The units of the output match the units in which the electromagnetic wavelength of the GPS signal λ is given (we have used mm).

The effect of the hydrometeors is not the only source of polarimetric phase shift. The GNSS satellites are supposed to transmit pure RHCP electromagnetic fields, but, as stated in the GPS interface control document (NAVSTAR GPS, 2015), a certain level of cross-polar transmission is tolerated. The slightly elliptical transmitted signals (ellipticity characterized by the ratio of circular cross-polar to circular co-polar amplitude m and the orientation of the main axis of the ellipse Δ) are then rotated

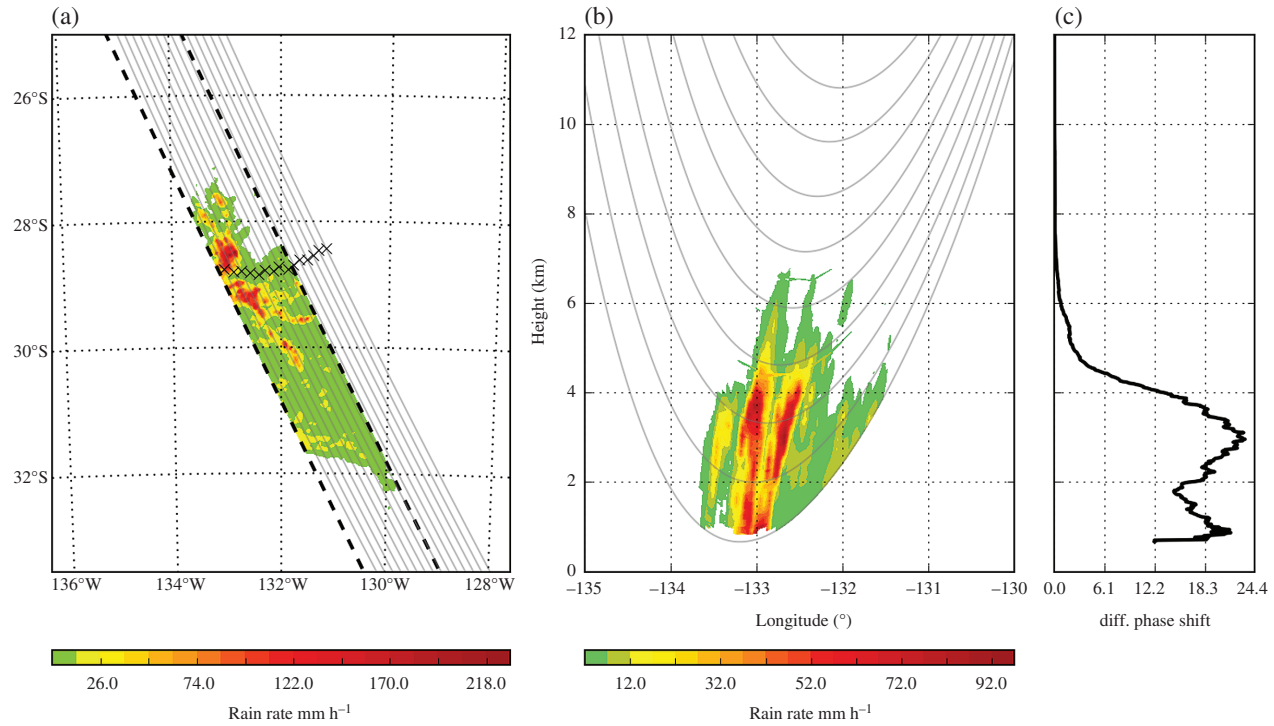

Figure 2. Example of artificial co-location between RO and GPM: (a) orbital swath of the GPM measurements together with the horizontal projection of some of the ray trajectories of a RO profile; the RO tangent points are indicated with 'x'. Note that the location of the RO rays does not correspond to any actual event, but is artificially translated to this location to guarantee full alignment with the GPM measurement. (b) Interpolation of the GPM rain-rate measurements into the ray trajectories (only a few rays are shown; in fact, there are ∼6000 rays in this RO event, ∼1200 of them at $h_t < 20$ km). (c) Hydrometeor component induced by the precipitation along each of the ∼6000 rays, as a function of the altitude of their tangent points. The reference LUTs are based on this type of artificial co-location, but only 80 rays (at 0.250 km vertical spacing) are considered. This exercise is repeated along all GPM orbits between 2015 and 2016, resulting in ∼250 000 PRO vertical profiles, of which ∼60 000 present some $\Delta\Phi_{hyd}(h_t)$ signature.

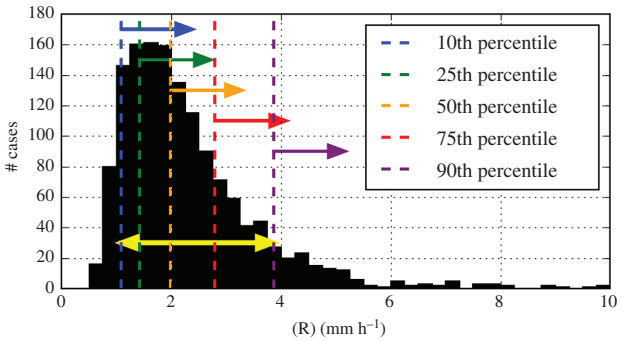

Figure 3. Histogram of one cell of the LUT grid: among the ∼250 000 vertical profiles of PRO observables generated with the artificial co-location, 1434 of them have one point of the profile within the cell defined as 1.5 mm $< \Delta\Phi_{hyd} \leq$ 2 mm and 1.5 km $< h_t \leq$ 1.75 km. This histogram shows the along-ray averaged rain rate of all these cases, as obtained from GPM CORRA interpolated data (see Figure 2(b)). The 10th, 25th, 50th, 75th and 90th percentiles are indicated. Note that for 75% of the time, an observable within this cell was induced by averaged rain rates larger than its 25th percentile (1.1 mm h^{-1}); it has 50% chance of coming from mean rain rates larger than 2 mm h^{-1} and the dispersion between its 10th and 90th percentiles is ∼3 mm h^{-1}. Most of the cells present a peak between the 25th and 50th percentile. The LUT^{Nth} stores, for each cell, the value of the Nth percentile of the distribution within that cell. We have generated LUTs for the 25th, 50th, 75th, 10th and 90th percentiles, as well as the LUT of the difference between the 10th and 90th percentiles. The most probable value R^*, for which a LUT is also generated, is obtained from the peak of the 0.25 mm h^{-1} binned histogram.

by Faraday effects during their way across the ionosphere. The Faraday rotation Ω is also a cumulative effect along the ray, where the electron density and the magnetic field determine its value at each point. Note that if the transmitted signals were purely circular, the Faraday rotation would not induce any differential phase shift between the two linear polarized components (both being affected identically). It is therefore useful to distinguish between the rotation suffered before reaching the precipitation cell (Ω_1, occurring at the right-hand side of Figure 1, between the transmitter and the lower troposphere) and that suffered after the precipitation cell (Ω_2, at the left-hand side of Figure 1, between the lower troposphere and the receiver). Finally, the receiver can also induce polarimetric shift, through the phase pattern of the receiving antenna and cabling and as an arbitrary initial phase ϕ_{arc} that the receiver sets at the beginning of each tracking arch (continuous segment of data).

We will assume that the phase pattern of the receiving antenna and cabling effects can be calibrated and that the remaining effects vary smoothly during the fraction of the RO profile that is affected by rain. Under these assumptions, we have shown that the total polarimetric phase shift measured above the rain can be extrapolated downwards to the surface and these extrapolated values can be used effectively as a correction term for the remaining systematic effects. This ad hoc separation technique will be used here to isolate $\Delta\Phi_{hyd}$, the parameter of interest, from the total measured phase shift: $\widetilde{\Delta\Phi_{hyd}}(h_t) = \Delta\Phi_{total}(h_t) - \Delta\Phi_{extrap}(h_t)$. In this study, the extrapolation is performed by first fitting a second-order polynomial to the measurements of phase shift between 70 and 18 km and then evaluating the polynomial at lower altitudes. This approach has been shown to provide a good separation of the hydrometeor term, provided that the Faraday rotation suffered after rain Ω_2 is small enough. Cases with $\Omega_2 < 15^\circ$ result in $\widetilde{\Delta\Phi_{hyd}}(h_t)$ with errors smaller than 10%. Based on actual ionospheric and Earth magnetic field values and the actual geometry of GNSS RO events co-located with TRMM measured precipitation, in 75% of the cases $\Omega_2 < 4.9^\circ$ and only in 3% of the cases $\Omega_2 > 15^\circ$. Therefore, the separation approach will provide $\widetilde{\Delta\Phi_{hyd}}(h_t) \approx \Delta\Phi_{hyd}(h_t)$ in most cases.

3. Generation of reference probability look-up tables

As described above, the GNSS PRO observable is the phase delay shift, here given in GPS L1-band millimetres, between the H and V polarizations of the received signal, from which the contribution due to hydrometeors $\Delta\Phi_{hyd}$ has been identified and separated

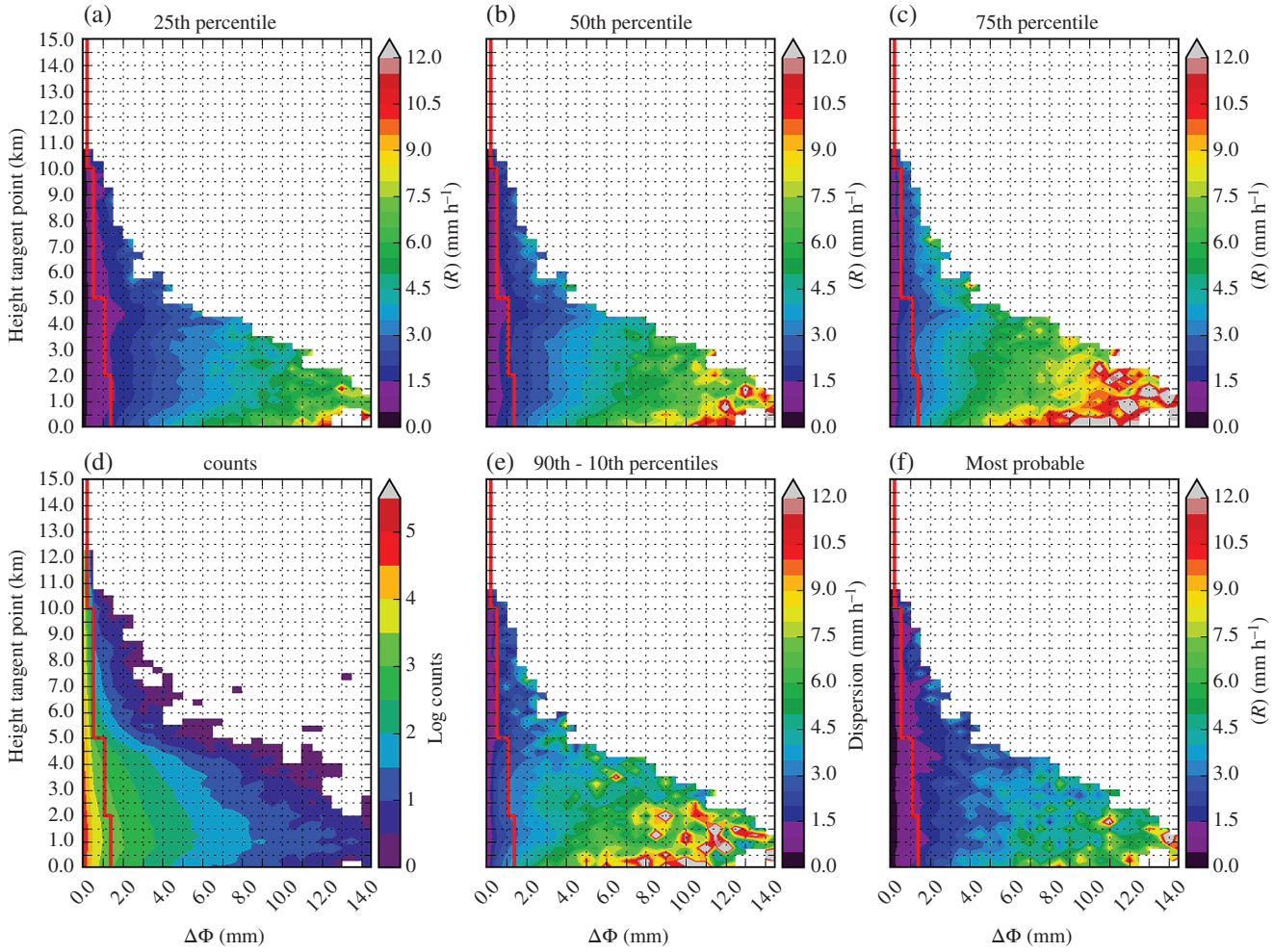

Figure 4. LUT generated with artificial co-locations with GPM CORRA products based on the along-ray averaged rain rate, $\langle R \rangle$. (a) 25th, (b) 50th and (c) 75th percentiles, with (d) number of cases, (e) dispersion, given as (90th−10th) percentiles, and (f) most probable along-ray mean rain rate $\langle R \rangle^*$. The thick red line shows the expected noise level of the measurement: observations below this threshold are masked by the noise and cannot be used.

through a simple algorithm. A time series of these observables is obtained for each particular radio-occultation event and each of the times of the series corresponds approximately to one altitude of the tangent point h_t (point of the radio link closest to the surface and with propagation direction parallel to it). This assumption fails when multiple atmospheric pathways are present, something that which we neglect at this stage. Hence, $\Delta\Phi_{hyd}(h_t) \equiv \Delta\Phi_{hyd}(t)$. In this section we develop a methodology to relate a given value of $\Delta\Phi_{hyd}(h_t)$ to probabilistic information about the rain cell that ray might have crossed. The methodology is based on look-up tables of maximum probability and several percentile occurrence values.

In order to generate the LUTs, the hydrometeor component of the polarimetric phase shift has been simulated for sets of RO ray trajectories that have been co-located artificially (i.e. the coincidence in space and time is forced) along the GPM satellite orbit, aligned with the satellite travel direction. The GPM combined algorithm (Ku-band radar plus radiometer) Version 4 data products (Grecu *et al.*, 2016), also identified as Combined Radar-Radiometer Algorithm (CORRA) products, are used to obtain a three-dimensional profile of the GPM products in the artificial RO plane. These products cover a 245 km swath and provide vertical profiles of the hydrometeor size distribution, phase, precipitation rate and condensed (ice, mixed or liquid phase) water content up to 20 km above the reference surface with 250 m vertical resolution. These data can be used to simulate GNSS observables in the L band. Note that these GPM CORRA products are not fully decoupled from actual GNSS RO measurements, as the retrieval algorithm uses information from models to apply certain corrections (e.g. path attenuation in Chandrasekar *et al.*, 2003). Since GNSS RO are assimilated into global weather models, indirect RO information may be embedded in the GPM products being used in this exercise. However, since we treat GPM CORRA products as our reference precipitation information in artificial (not actual) RO events, any potential correlation between the GPM product and actual GNSS ROs would have little effect on the polarimetric retrieval.

Here 'artificial' co-location is understood as a synthetic RO event that occurs within the swath of the GPM observations (artificially co-located in space and time). The simulated RO rays are only used to generate the polarimetric response from propagating through hydrometeors as retrieved from GPM, but there are no actual RO thermodynamic soundings derived from these (synthetic) rays. Finally, the hydrometeor component of the polarimetric phase shift is computed along each synthetic ray to simulate the observable $\Delta\Phi_{hyd}(h_t)$ following Eq. (1). A total of 80 rays in each RO event are considered, at 0.250 km spacing between their tangent points ($\Delta h_t = 0.250$ km) covering an altitude range of 0–20 km. This vertical sampling is consistent with the integration needed to increase the signal-to-noise ratio (SNR) of the measurement and decrease the noise of the phase delay observables down to the required 1–1.5 mm (Cardellach *et al.*, 2015). Here, the artificial co-location is chosen to increase the statistics and thus obtain a more robust probabilistic characterization. An example of an artificial co-location, its interpolation of the precipitation information and final hydrometeor observables is shown in Figure 2. The exercise, using GPM CORRA data over two years (2015–2016), resulted in ∼250 000 PRO vertical profiles, of which ∼60 000 have at least one RO ray crossing a precipitation cell and ∼14 000 induce polarimetric phase shifts above the expected noise level. Note that

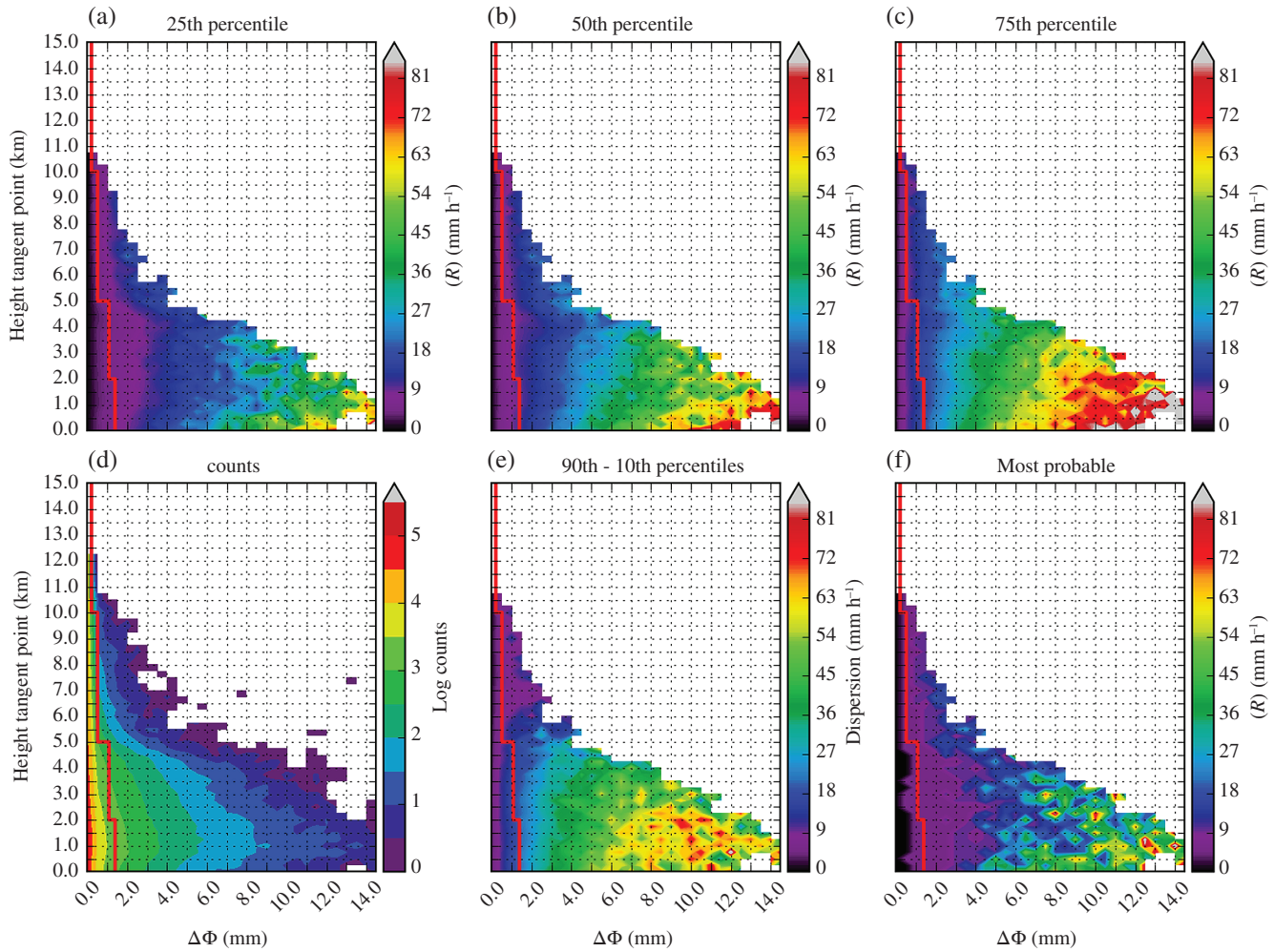

Figure 5. Same as Figure 4 but based on the maximum rain-rate value along the RO ray, R_{max}: (a) 25th, (b) 50th and (c) 75th percentiles, with (d) number of cases, (e) dispersion, given as (90th−10th) percentiles, and (f) most probable along-ray maximum rain rate R^*_{max}. The thick red line shows the expected noise level of the measurement: observations below this threshold are masked by the noise and cannot be used.

actual −non artificial −spatio-temporal co-locations will be used in section 4 to test the performance of the LUT methodology.

The LUTs are defined over a grid on to the 2D space of $(\Delta\Phi_{hyd}, h_t)$, with cell resolutions of 0.5 mm in polarimetric phase delay shift and 250 m in altitude. We want to characterize statistically the rain that induced $\Delta\Phi_{hyd}(h_t)$ observables within each cell. The rain information is obtained from the GPM CORRA products used to simulate the observables. The characterization is done through several probabilistic parameters of two variables: the along-ray mean values of the GPM rain rates $\langle R\rangle$ and the maximum GPM rain-rate value along the ray R_{max}. The probabilistic parameters are the *most probable* and a set of *percentiles*. For example, the 75% of time that an observable has a value within the cell $(\Delta\Phi^i_{hyd}, h^j_t)$ will correspond to $\langle R\rangle$ larger than the corresponding $\langle R\rangle^{25th}_{ij}$ percentile. To illustrate this step, Figure 3 shows the histogram of one particular cell of the LUT grid and its relevant percentiles. The methodology has been applied to the 25th, 50th and 75th percentiles (different LUTs, one for each percentile), as well as to the difference between the 10th and 90th percentiles. The latter gives an idea of the dispersion within each cell. To obtain the most probable value within each cell $R^*(\Delta\Phi^i_{hyd}, h^j_t)$, a histogram is first generated to pick the rain rate of maximum probability. The histograms are generated at 0.25 mm h^{-1} binning for along-ray averaged rain rate and 5 mm h^{-1} along-ray maximum rain rate. The larger the binning size, the coarser the resolution of R^*, but the more robust the solution.

Figures 4 and 5 show the LUTs generated for the averaged rain rate $\langle R\rangle$ and the maximum rain rate R_{max}, respectively. The plots also show the expected noise level in a ROHP−PAZ-like experiment. These are the reference tables for the assessment conducted in section 4.

These types of LUT have also been generated for different regions and seasons. The regional effects are noticeable, especially the distinction between tropical and extratropical features, while the seasonal effects are secondary. In general, a much larger number of events is required to build regional and seasonal LUTs so that each of the LUTs has a statistically significant number of cases within each cell. Note that certain cells of the global LUTs shown in Figures 4 and 5 present a relatively low population of cases. It must also be noted that the LUTs, being generated from GPM data, thereby carry the sampling characteristics of those sensors, with the higher latitudes over-represented relative to the equatorial latitudes.

4. Validation by end-to-end simulations

In this section we validate the LUT inversion approach by applying it to a set of realistic synthetic data. The synthetic data correspond to actual co-locations between *COSMIC/FORMOSAT-3* (COSMIC hereafter) RO events and TRMM precipitation 3D measurements (TRMM 2A25 products). A co-location is identified when the COSMIC RO event has its 10 km altitude tangent point within the TRMM swath. This realistic co-location exercise has resulted in 550 profiles with intense rain rates from 2006−2016.

The data synthesis is performed by means of an end-to-end simulation that includes all the terms summarized in section 2, where the ionospheric electron content is extracted from the

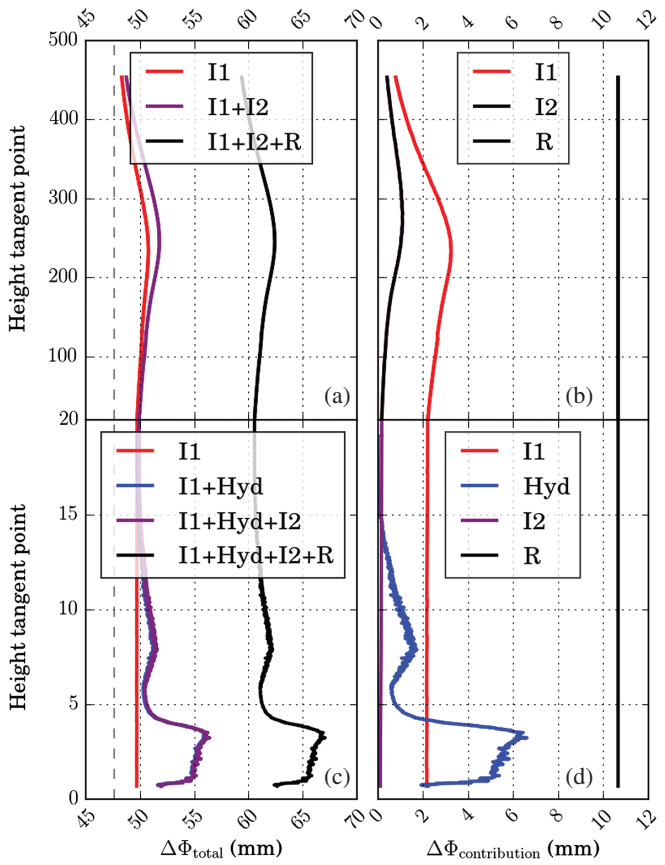

Figure 6. Example of total observed polarimetric phase shift $\Delta\Phi$ as a function of each ray's tangent point altitude and its individual contributions, including transmitter effects, ionosphere before precipitation (I1), ionosphere after precipitation (I2) and arbitrary initial phase shift and antenna pattern in the receiver (R). The term of interest is the hydrometeor one, which must be separated from the rest of the terms. (a) and (b) correspond to altitudes above 20 km, while (c) and (d) show altitudes below 20 km. (a) and (c) show the partial cumulative effects of the different factors: in red the effects of the transmitter and I1; in blue the hydrometeor component is added; the ionosphere after rain is added in the purple line; and finally the total observed $\Delta\Phi$ is in black, also including receiver effects. The grey dashed line around 47.6 mm corresponds to pure RHCP transmission. (b) and (d) show four contributions separately.

IRI-2012 model (International Reference Ionosphere: Bilitza *et al.*, 2014), the magnetic field from the IGRF-12 model (International Geomagnetic Reference Field: Thébault *et al.*, 2015) and the ellipticity of the transmitted signal is assumed to be at $m = 0.1$ level (10% of left-hand circularly polarized signals) within the GPS requirements (NAVSTAR GPS, 2015), with an arbitrary orientation angle Δ of random value. The receiving antenna effects are assumed to be calibrated, except for its initial polarimtric shift (ϕ_{arc}, an arbitrary number between the phase-delay measurements of the H and V channels of the receiver), which is data-arch dependent, i.e. different ϕ_{arc} for each set of continuously acquired observations. It is set to 60°. The ionospheric effects I_1 and I_2, induced by Faraday rotations Ω_1 and Ω_2 due to ionosphere crossed before and after the precipitation cell, respectively, are also included in the E2E simulation. An example of the vertical profile of the total polarimetric shift observation is shown as a black line in the left panel of Figure 6.

The simple separation algorithm presented in section 2 is then applied to isolate the hydrometeor component (blue line in right panel of Figure 6) from the total measurement (black line in left panel of Figure 6). The algorithm takes advantage of the fact that the ionospheric, transmitter and receiver effects are smoothly evolving in the bottom layers of the atmosphere, where the rain is sensed. Therefore the separation is not perfect and in some cases the isolated hydrometeor component $\widetilde{\Delta\Phi_{\text{hyd}}}(h_t)$ (tilde used to distinguish it from the actual hydrometeor component $\Delta\Phi_{\text{hyd}}(h_t)$) will be contaminated by mis-correction terms (see validity of the separation algorithm at the end of section 2). With the hydrometeor term isolated, it is possible to apply the LUT retrieval approach: that is, extract from the LUTs those values corresponding to each $\widetilde{\Delta\Phi_{\text{hyd}}}(h_t)$ in the data. These sets of values will provide, at each altitude of the PRO profile, the most probable rain rate, together with the rain rate of 25th, 50th and 75th percentiles and the dispersion (10th–90th percentile difference).

Given that the actual rain is well known in synthetic data, we can validate the output of this probabilistic retrieval with the actual values of the rain that induced the polarimetric signals. Nevertheless, the validation cannot be based on individual cases, as the retrieval approach provides a set of probabilities of rain rates. The validation can only be performed by comparing the actual distribution of rain rates to which our approach has assigned the same set of percentiles, i.e. comparing the original LUTs with the statistics of the TRMM rain rates that induced the synthetic $\widetilde{\Delta\Phi_{\text{hyd}}}(h_t)$. Note that this is equivalent to generating a new set of LUTs, now from the end-to-end simulation (LUT_{e2e}). The differences between the reference LUTs developed in section 3 (LUT_{ref}) and the statistics of the end-to-end simulation exercise (LUT_{e2e}) can be understood as the error of this probabilistically based retrieval approach. Note that only the hydrometeor component was generated in LUT_{ref}, while all terms are synthesized and then a separation algorithm is applied to isolate the hydrometeor component in LUT_{e2e}.

These differences are shown in Figure 7. The cells populated in both LUT_{ref} and LUT_{e2e} (the only cells that can be compared) agree better than $\pm 1\,\text{mm}\,\text{h}^{-1}$ rain rate in 57–60% of the cells. When noise is added to the synthetic data of the end-to-end simulations, the comparison shown in Figure 8 is achieved. The noise added is that expected for the GNSS PRO in the ROHP–PAZ experimental set-up (Cardellach *et al.*, 2015): it is related to the SNR of the actual COSMIC data and degraded to account for the 3 dB loss due to the mismatch between the circularly polarized transmitted field and the linearly polarized receiving antenna. The difference in this case is better than $\pm 1\,\text{mm}\,\text{h}^{-1}$ in 58–67% of cells. Only observations with actual SNR above the noise level are considered in the statistics. Table 1 details several parameters of this comparison, by means of the weighted mean and standard deviation of the differences between the realistic LUT_{e2e} and the reference LUT_{ref}. The statistics with and without noise are similar, with the noise reducing the overall biases by balancing the cells with positive biases with those of negative biases. The dispersion in both noise-free and noisy scenarios is generally better than $1\,\text{mm}\,\text{h}^{-1}$ root-mean-squared difference. A systematic under-representation of the rain above 6 km altitude is seen in the results with added noise, with more blue colour at higher altitudes. This under-representation can be due to false positives induced by the noise. However, these blue cells have little weight in the average, as they correspond to cells of much lower population than the cells close to zero rain rate, as seen in the last three columns of Table 1. Remarkably, the biases do not exceed $1.12\,\text{mm}\,\text{h}^{-1}$, with the statistics of the end-to-end simulations generating higher rain rates than the statistics of the reference LUTs. Possible reasons for this positive bias would include the following: (i) the residual effects of the separation algorithm; (ii) the fact that the 550 COSMIC-TRMM co-locations in LUT_{e2e} correspond to the most extreme cases; (iii) the different sensitivity to light rain as provided by the TRMM and GPM CORRA products used in this study (GPM radar and radiometric combined products have been used in this study for the generation of LUT_{ref}, while TRMM radar-only products are used to generate LUT_{e2e}); and (iv) incomplete co-locations between TRMM and COSMIC GNSS RO profiles used in the study (partially out of the TRMM swath).

5. Application

In the previous sections we have first generated a suite of reference LUTs based on hydrometeor-induced phase shift in GNSS PRO

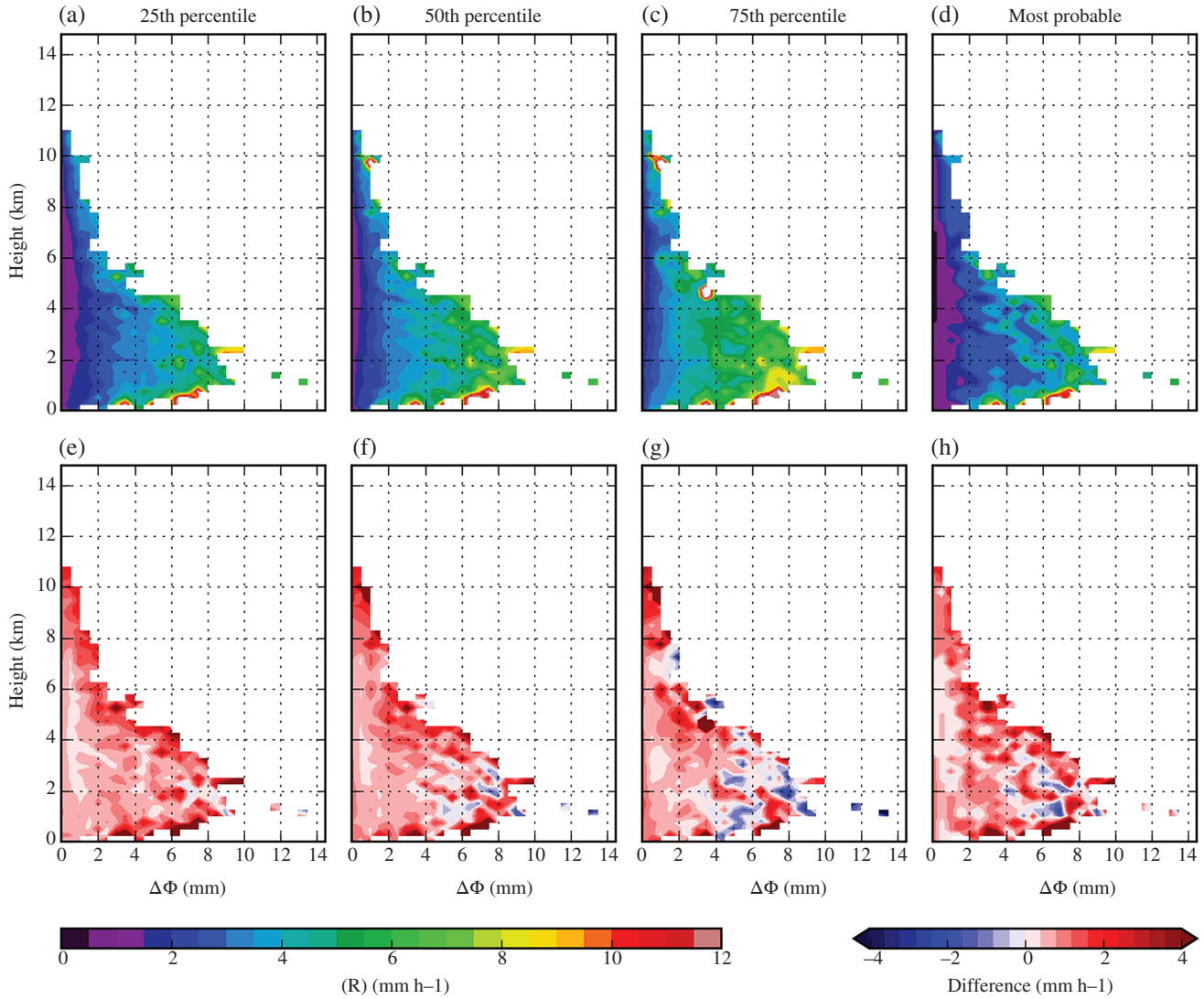

Figure 7. Comparison between the reference LUTs in Figure 4 and the statistics of $\widetilde{\Delta\Phi_{hyd}}(h_t)$ as generated from actual co-locations between COSMIC and TRMM missions, taking into account transmitter, ionospheric, hydrometeor and receiver effects and isolating the hydrometeor component after a simple algorithm (LUT_{e2e}: (a)–(d)). The bottom row (e–h) is the difference $LUT_{e2e}-LUT_{ref}$: (e) LUT^{25th}, (f) LUT^{50th}, (g) LUT^{75th} and (h) most probable LUT^{*}, respectively.

(section 3) and later assessed the probabilistic errors introduced by other systematic effects, such as transmitter ellipticity and orientation, the ionosphere before and after the hydrometeor depolarization and receiver phase shifts (section 4). In this section we present illustrative examples of the applicability of this LUT methodology to extract precipitation information in the upcoming ROHP–PAZ GNSS PRO data. Given that the *PAZ* satellite has not been launched and there is no other GNSS PRO mission in orbit, the polarimetric part of this exercise is based on synthetic data.

The complete GNSS PRO polarimetric phase shift observable $\Delta\Phi(h_t)$ has been synthesized with the end-to-end simulator for a set of COSMIC RO events co-located with TRMM and its hydrometeor component has been isolated using the algorithm presented in section 2. The isolated hydrometeor component $\widetilde{\Delta\Phi_{hyd}}(h_t)$ is then searched for through the reference LUT tables developed in section 3 (generated with artificial co-locations with the GPM CORRA products and accounting only for the hydrometeor contribution). As a result of this interrogation, for each altitude h_t we obtain the most probable along-ray maximum and averaged rain rates, as well as their 10th, 25th, 50th, 75th and 90th percentiles. That is, we obtain the probabilistic expectation of rain at each altitude. In fact, this is not the only information to be obtained from the GNSS PRO, as the data can also be processed using the standard non-polarimetric technique to extract the thermodynamic vertical profiles. Therefore, the selected cases shown in Figure 9 illustrate the overall outcome of GNSS PRO events: their thermodynamic sensing and their precipitation probabilistic characterization. In the examples provided here, the thermodynamic profiles correspond to the actual measurements of the COSMIC selected events as provided by the University Corporation for Atmospheric Research (UCAR), while the probabilistic characterization of the precipitation is based on the LUT-based inversion of the synthetic data generated by end-to-end simulations, including random noise. The selected thermodynamic products are the temperature and relative and specific humidity profiles, obtained at UCAR using the European Centre for Medium-Range Weather Forecasts (ECMWF) Re-Analysis (ERA) Interim (Dee *et al.*, 2011) as a first guess in the processing. Among the COSMIC/TRMM co-located events that have been simulated from end to end, the precipitation retrievals of those with the highest hydrometeor component are included as File S1, available on-line at the QJRMS site (92 profiles). In Figure 9, the thermodynamic and precipitation profiles do not reach the same bottom levels, because (i) we have only simulated a subset of the total observed RO rays, (ii) the polarimetric measurement in these low regions might be masked by larger noise and then is not shown in our results, and (iii) in given cases, TRMM does not provide rain measurements at the lowest bins.

6. Discussion

This study has presented a methodology to retrieve intense precipitation information from polarimetric GNSS RO observables.

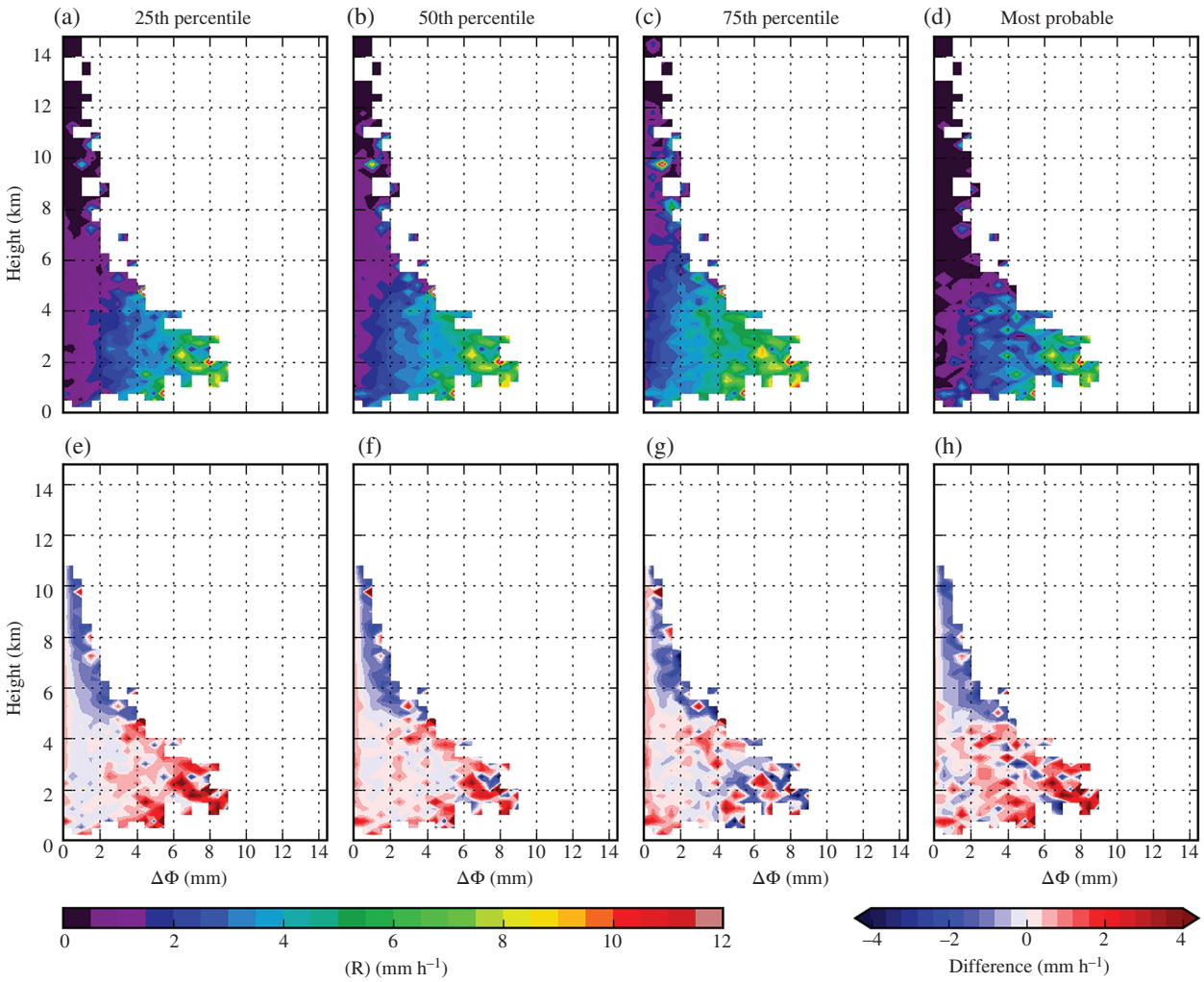

Figure 8. Same as Figure 7 but after adding noise to the end-to-end simulated data.

Table 1. Comparison between the reference LUTs generated with $\Delta\Phi_{hyd}(h_t)$ obtained from artificial co-locations between RO and GPM (section 3) and the LUTs generated with $\widetilde{\Delta\Phi}_{hyd}(h_t)$, after an end-to-end data synthesis and a simple algorithm to separate the hydrometeor component (section 4).

Comparison	Overall difference	$h_t = 2 \pm 1$ km	$h_t = 4 \pm 1$ km	$h_t = 8 \pm 1$ km
$LUT^{25th}_{e2e} - LUT^{25th}_{ref}$	0.67 ± 0.41	0.60 ± 0.35	0.53 ± 0.29	0.90 ± 0.18
$LUT^{50th}_{e2e} - LUT^{50th}_{ref}$	0.76 ± 0.53	0.63 ± 0.43	0.64 ± 0.31	0.92 ± 0.28
$LUT^{75th}_{e2e} - LUT^{75th}_{ref}$	0.82 ± 0.86	0.55 ± 0.62	0.70 ± 0.76	1.12 ± 0.41
$LUT^{*}_{e2e} - LUT^{*}_{ref}$	0.39 ± 0.63	0.52 ± 0.66	0.23 ± 0.53	0.79 ± 0.42
$LUT^{25th}_{e2e+noise} - LUT^{25th}_{ref}$	-0.02 ± 0.66	-0.04 ± 0.78	-0.05 ± 0.59	0.08 ± 0.78
$LUT^{50th}_{e2e+noise} - LUT^{50th}_{ref}$	0.10 ± 0.70	0.05 ± 0.65	0.10 ± 0.62	0.28 ± 0.86
$LUT^{75th}_{e2e+noise} - LUT^{75th}_{ref}$	0.16 ± 0.88	-0.15 ± 0.87	0.10 ± 0.83	0.34 ± 1.07
$LUT^{*}_{e2e+noise} - LUT^{*}_{ref}$	-0.04 ± 0.86	-0.27 ± 1.19	-0.03 ± 0.92	0.04 ± 0.88

The mean and standard deviation of the differences are weighted based on the population of each cell. Differences averaged across the whole LUT and also by altitude are given in different columns. All units in mm h^{-1}.

The retrieval technique characterizes the probability of rain rate by interrogating the polarimetric observables with a suite of reference look-up tables. The LUTs have been generated with artificial co-locations between GNSS RO ray trajectories and the measurements from the GPM mission (section 3). The method has been validated thereafter, also in statistical terms, with more realistic synthetic data from actual co-locations between the *COSMIC/FORMOSAT-3* GNSS RO mission and the TRMM precipitation mission (section 4). In addition to polarimetric effects due to hydrometeors intersecting the GNSS radio links, the polarimetric impurity of transmitted signals (within GPS official requirements), the ionosphere and Earth's magnetic field and the receiver instrumental effects have been accounted for in the validation exercise, where a simple separation algorithm has been implemented to isolate the hydrometeor component from the remaining systematic effects (summarized in section 2). This work details neither the whole propagation issue nor the theoretical basis of the separation algorithm, as these topics are tackled in a separate work and are not the main focus of the study.

The main focus is the probabilistic retrieval approach, which uses the heritage of the GPM mission as a reference statistical frame. The GPM-based LUTs have been shown to be valuable tools to invert probabilistic features of the intense rain crossed by GNSS PRO observations, as, within each cell, the statistics obtained with actual co-locations matched the statistics of the reference tables to better than 1 mm h^{-1}. A positive bias of the order of $\leq$1 mm h^{-1} has also been reported in the noise-free runs, which tends to zero when noise is added. The sign of the biases is consistent with distributions of the actual co-locations presenting slightly higher values of the rain rates than the reference distributions. This could be the combined effect of three aspects of the exercise: residual systematic effects after the separation algorithm; the sampling of the actual co-location (based on 550 co-locations of high-intensity and extreme events); and potential differences in sensitivity to light precipitation between the TRMM measurements used in the validation and the GPM CORRA combined products used to build the reference LUTs. The methodology would benefit from extending the number of cases compiled in the reference LUTs, especially for those cells of the LUT that are poorly populated. Extending the number of cases would also permit the generation of LUTs constrained by regional and seasonal criteria. A self-consistent extension of the LUTs is feasible as the GPM mission continues its operations.

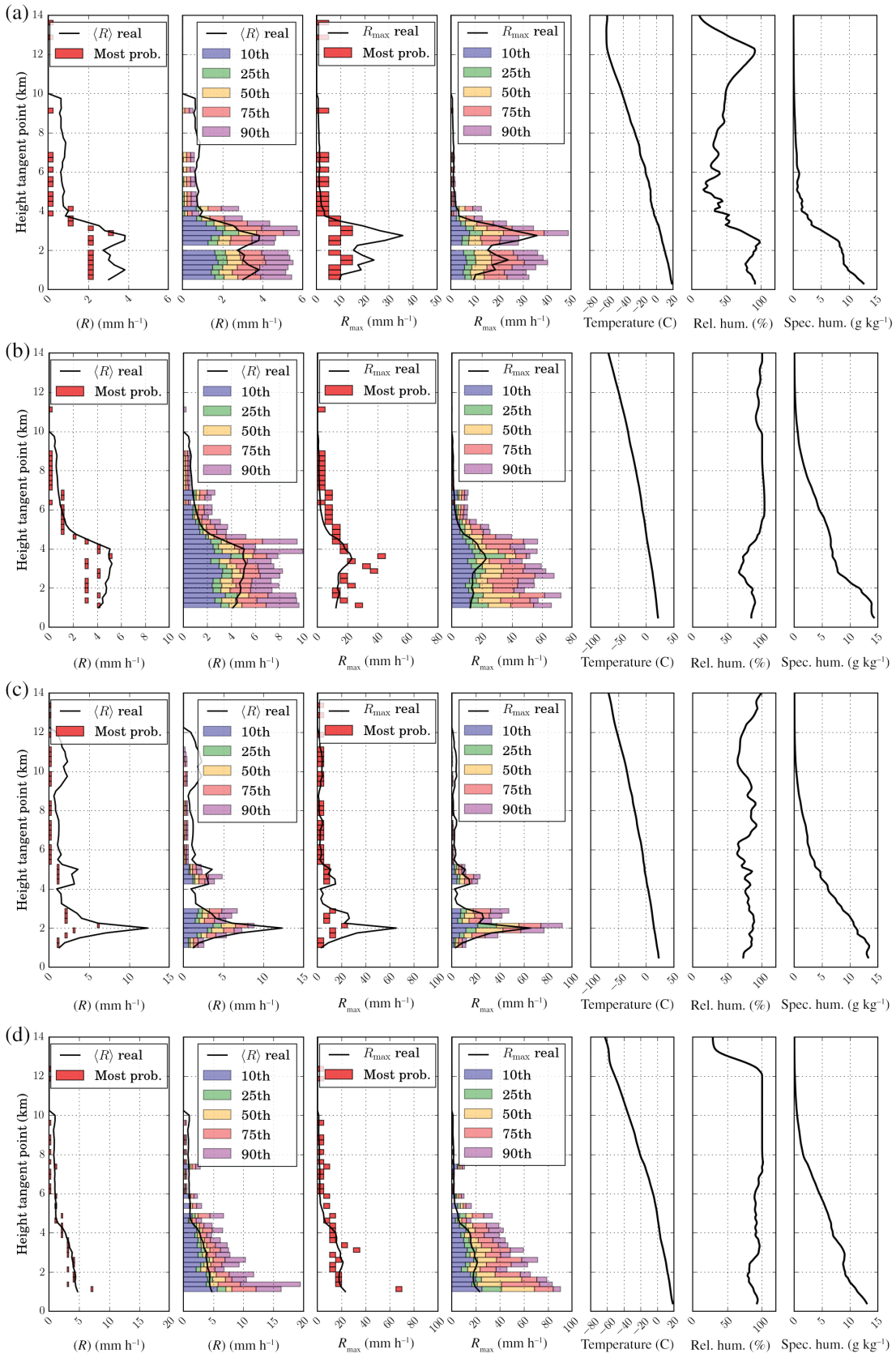

Figure 9. Examples of application of the LUT methodology in four RO cases to obtain a complete set of GNSS PRO products. The cases correspond to actual COSMIC RO events co-located with TRMM precipitation measurements. The thermodynamic products are provided by the standard processing of GNSS RO, while the synthetic polarimetric observables were here generated by end-to-end simulations of these events and then inverted to the most probable and percentile rain-rate values using the LUTs. In the four leftmost columns, we present the probabilistic retrievals for the most probable along-ray averaged rain rate, along-ray averaged rain-rate percentiles, most probable along-ray maximum rain rate and along-ray maximum rain-rate percentiles. The black line corresponds to the actual TRMM values. In the three rightmost columns, we show the actual thermodynamic vertical profiles measured with COSMIC: refractivity, temperature and mixing ratio as provided by UCAR. The COSMIC RO events, identified as in the UCAR system, and their locations are, from top to bottom: C001.2011.051.06.35.G07 (S23.2°, W160.7°), C001.2008.035.10.26.G03 (N34.8°, E137.5°), C004.2008.170.20.35.G26 (N15.1°, E98.0°) and C004.2008.343.22.42.G14 (N23.4°, E133.2°).

The probabilistic retrievals could be complemented, in some cases, with alternative inversion approaches (e.g. the tomographic technique tested in Padullés *et al.*, 2016b). These approaches, or others based on data assimilation schemes, could help in dealing with the coarse horizontal resolution of the measurement, which may be integrating hydrometeor information over a few hundred kilometres (see Figure 2). We must note, however, that similar resolution issues are found in standard RO measurements, especially for water-vapour structures, yet comparisons of RO with the finer resolution radiosonde measurements show strong agreement (e.g. Kuo *et al.*, 2005). Moreover, dependence of convective onset statistics on spatial averaging has been quantified for the case where column water vapour (for a given bulk temperature) is used as a leading environmental variable (Schiro *et al.*, 2016) and the rapid increase of conditional average precipitation and probability of precipitation that characterizes the onset of conditional instability is robust for spatial averaging in retrievals from 0.25° to about 2° latitude–longitude boxes. This is principally because the water-vapour environment has high spatial autocorrelation on these horizontal scales (and temperature in the free troposphere has even larger typical spatial scales). Thus the spatial footprint of the RO is expected to give a good measure of the vertical structure of the convective environment. Therefore, in general the horizontal resolution should not be a dominant effect, except for very specific studies, where small structures are the objective of the analysis.

Given that the GNSS PRO observations are also suitable for standard GNSS RO retrievals, this study has presented a more complete product of the GNSS PRO measurements, here illustrated with a few examples in section 5 and more than 90 others in File S1. The complete set of products includes vertical profiles of thermodynamical variables in addition to vertical profiles of rain-rate probabilities. This GNSS PRO product is rather unique, as there is no single instrument that can provide this set of vertical profiles across heavy precipitation cells. Moreover, temperature profiles obtained with the GNSS RO standard techniques will also complement the polarimetric ones by helping to distinguish between vertical layers with liquid precipitation and those with frozen hydrometeors. The technique could therefore contribute to filling the gap in current satellite observations of moisture structure during heavy precipitation conditions. This information provides other potential benefits: for example, to improve and evaluate the cloud microphysical parametrizations used in NWP forecast models and to understand cloud processes and thermodynamic conditions within convective cloud structures better.

Acknowledgements

This study used data from the *COSMIC/FORMOSAT-3*, TRMM and GPM missions. Data from TRMM and GPM missions can be accessed through https://storm.pps.eosdis.nasa.gov/. The ionospheric information used in the simulations has been obtained from the International Reference Ionosphere (IRI) and the terrestrial magnetic field from the 12th Generation of International Geomagnetic Reference Field (IGRF). The work performed by E. Cardellach, R. Padullés and S. Tomás has been supported by the Spanish Grant ESP2015-70014-C2-2-R. Part of E. Cardellach's contribution has been supported by the Radio Occultation Meteorology Satellite Application Facility (ROM SAF), which is a decentralised operational RO processing centre under *EUMETSAT*. Work performed by F. J. Turk, C. O. Ao and M. de la Torre was carried out at the Jet Propulsion Laboratory, California Institute of Technology, under a contract with the National Aeronautics and Space Administration, with support from the NASA Earth Science US Participating Investigator Program for the PAZ–ROHP mission, grant NNH14ZDA001N-ESUSPI.

Supporting information

The following supporting information is available as part of the online article:

File S1. A set of complementary examples as the one shown in Figure 9. They correspond to the synthetic PRO products from 92 co-locations between COSMIC RO and TRMM precipitation missions.

References

Anthes RA, Ector DD, Hunt DC, Kuo YH, Rocken CC, Schreiner WS, Sokolovskiy SV, Syndergaard SS, Wee TK, Zeng ZZ, Bernhardt PA, Dymond KF, Chen YY, Liu HH, Manning KK, Randel WJ, Trenberth KE, Cucurull L, Healy SB, Ho SP, McCormick CC, Meehan TK, Thompson DC, Yen NL. 2008. The COSMIC/FORMOSAT-3 mission: Early results. *Bull. Am. Meteorol. Soc.* **89**: 313–333. https://doi.org/10.1175/BAMS-89-3-313.

Battaglia A, Tanelli S, Mroz K, Tridon F. 2015. Multiple scattering in observations of the GPM dual-frequency precipitation radar: Evidence and impact on retrievals. *J. Geophys. Res.: Atmos.* **120**(9): 4090–4101 https://doi.org/10.1002/2014JD022866.

Battaglia A, Mroz K, Tanelli S, Tridon F, Kirstetter P. 2016. Multiple-scattering-induced 'Ghost Echoes' in GPM DPR observations of a tornadic supercell. *J. Appl. Meteorol. Climatol.* **55**: 1653–1666. https://doi.org/10.1175/JAMC-D-15-0136.1.

Bilitza D, Altadill D, Zhang Y, Mertens C, Truhlik V, Richards P, McKinnell L-A, Reinisch B. 2014. The International Reference Ionosphere 2012 –a model of international collaboration. *J. Space Weather Space Clim.* **4**: A07. https://doi.org/10.1051/swsc/2014004.

Bringi VN, Chandrasekar VV, Balakrishnan NN, Zrni DS. 1990. An examination of propagation effects in rainfall on radar measurements at microwave frequencies. *J. Atmos. Oceanic Technol.* **7**: 829–840. https://doi.org/10.1175/1520-0426(1990)007⟨0829:AEOPEI⟩2.0.CO;2.

Cardellach E, Tomás S, Oliveras S, Padullés R, Rius A, de la Torre-Juárez M, Turk FJ, Ao CO, Kursinski ER, Schreiner B, Ector DD, Cucurull L. 2015. Sensitivity of PAZ LEO polarimetric GNSS radio-occultation experiment to precipitation events. *IEEE Trans. Geosci. Remote Sens.* **53**: 190–206. https://doi.org/10.1109/TGRS.2014.2320309.

Cardinali C, Healy SB. 2014. Impact of GPS radio occultation measurements in the ECMWF system using adjoint-based diagnostics. *Q. J. R. Meteorol. Soc.* **140**: 2315–2320. https://doi.org/10.1002/qj.2300.

Chandrasekar V, Fukatsu H, Mubarak K. 2003. Global mapping of attenuation at Ku- and Ka-band. *IEEE Trans. Geosci. Remote Sens.* **41**: 2166–2176.

Cunha LK, Smith JA, Baeck ML, Krajewski WF. 2013. An early performance evaluation of the NEXRAD dual-polarization radar rainfall estimates for urban flood applications. *Weather and Forecasting* **28**: 1478–1497. https://doi.org/10.1175/WAF-D-13-00046.1.

Dai A. 2006. Precipitation characteristics in eighteen coupled climate models. *J. Clim.* **19**: 4605–4630.

Dee DP, Uppala SM, Simmons AJ, Berrisford P, Poli P, Kobayashi S, Andrae U, Balmaseda MA, Balsamo G, Bauer P, Bechtold P, Beljaars ACM, van de Berg L, Bidlot J, Bormann N, Delsol C, Dragani R, Fuentes M, Geer AJ, Haimberger L, Healy SB, Hersbach H, Hólm EV, Isaksen L, Kallberg P, Köhler M, Matricardi M, McNally AP, Monge-Sanz BM, Morcrette J-J, Park B-K, Peubey C, de Rosnay P, Tavolato C, Thépaut J-N, Vitart F. 2011. The ERA-interim reanalysis: Configuration and performance of the data assimilation system. *Q. J. R. Meteorol. Soc.* **137**: 553–597. https://doi.org/10.1002/qj.828.

Derbyshire SH, Beau I, Bechtold P, Grandpeix J-Y, Piriou J-M, Redelsperger J-L, Soares PMM. 2004. Sensitivity of moist convection to environmental humidity. *Q. J. R. Meteorol. Soc.* **130**: 3055–3079.

Durden SL, Tanelli S. 2008. Predicted effects of nonuniform beam filling on GPM radar data. *IEEE Geosci. Remote Sens. Lett.* **5**: 308–310. https://doi.org/10.1109/LGRS.2008.916068.

Grecu M, Olson W, Munchak S, Ringerud S, Liao L, Haddad Z, Kelley B, McLaughlin S. 2016. The GPM combined algorithm. *J. Atmos. Oceanic Technol.* **33**: 2225–2245. https://doi.org/10.1175/JTECH-D-16-0019.1.

Hartmann DL, Klein Tank AMG, Rusticucci M, Alexander LV, Brönnimann S, Charabi Y, Dentener FJ, Dlugokencky EJ, Easterling DR, Kaplan A, Soden BJ, Thorne PW, Wild M, Zhai PM. 2013. 'Observations: Atmosphere and surface'. In *Climate Change 2013: The Physical Science Basis. Contribution of Working Group I to the Fifth Assessment Report of the Intergovernmental Panel on Climate Change*, Stocker TF, Qin D, Plattner G-K, Tignor M, Allen SK, Boschung J, Nauels A, Xia Y, Bex V, Midgley PM. (eds.): Chapter 2, pp 159–254, Cambridge University Press: Cambridge, UK and New York, NY.

Healy SB, Haase J, Lesne O. 2002. Abel transform inversion of radio occultation measurements made with a receiver inside the Earths atmosphere. *Ann. Geophys.* **20**: 1253–1256.

Hou AY, Kakar RK, Neeck S, Azarbarzin AA, Kummerow CD, Kojima M, Oki R, Nakamura K, Iguchi T. 2014. The global precipitation measurement mission. *Bull. Am. Meteorol. Soc.* **95**: 701–722. https://doi.org/10.1175/BAMS-D-13-00164.1.

Jin S, Cardellach E, Xie F. 2014. *GNSS Remote Sensing: Theory, Methods and Applications*, Remote Sensing and Digital Image Processing **19**. Springer-Verlag New York, NY; London. https://doi.org/10.1007/978-94-007-7482-7.

Kummerow CD, Randel DL, Kulie M, Wang N-Y, Ferraro R, Munchak SJ, Petkovic V. 2015. The evolution of the Goddard profiling algorithm to a fully parametric scheme. *J. Atmos. Oceanic Technol.* https://doi.org/10.1175/JTECH-D-15-0039.1.

Kunkel KE, Karl TR, Brooks H, Kossin J, Lawrimore JH, Arndt D, Bosart L, Changnon D, Cutter SL, Doesken N. 2013. Monitoring and understanding trends in extreme storms: State of knowledge. *Bull. Am. Meteorol. Soc.* **94**: 499–514.

Kuo Y-H, Schreiner WS, Wang J, Rossiter DL, Zhang Y. 2005. Comparison of GPS radio occultation soundings with radiosondes. *Geophys. Res. Lett.* **32**: L05817. https://doi.org/10.1029/2004GL021443.

Kursinski RE, Hajj GA, Schofield JT, Linfield RP, Hardy KR. 1997. Observing Earth's atmosphere with radio occultation measurements using the Global Positioning System. *J. Geophys. Res.* **102**: 23 429–23 465.

Lee IT, Tsai HF, Liu JY, Lin CH, Matsuo T, Chang LC. 2013. Modeling impact of FORMOSAT-7/COSMIC-2 mission on ionospheric space weather monitoring. *J. Geophys. Res.–Space* **118**: 6518–6523. https://doi.org/10.1002/jgra.50538.

Liu C, Zipser EJ, Cecil DJ, Nesbitt SW, Sherwood S. 2008. A cloud and precipitation feature database from nine years of TRMM observations. *J. Appl. Meteorol. Climatol.* **47**: 2712–2728. https://doi.org/10.1175/2008JAMC1890.1.

Masunaga H. 2014. Free-tropospheric moisture convergence and tropical convective regimes. *Geophys. Res. Lett.* **41**: N23. https://doi.org/10.1002/2014GL062301.

NAVSTAR Global Positioning Systems Directorate. 2015. 'NAVSTAR GPS space segment/navigation user segment interfaces IS-GPS-200'. Ref. IRN-IS-200H-003, version 9 December 2015. http://www.gps.gov/technical/icwg/ (accessed 20 October 2017).

Nesbitt SW, Cifelli R, Rutledge SA. 2006. Storm morphology and rainfall characteristics of TRMM precipitation features. *Mon. Weather Rev.* **134**: 2702–2721.

Padullés R, Cardellach E, de la Torre Juárez M, Tomás S, Turk FJ, Oliveras S, Ao CO, Rius A. 2016a. Atmospheric polarimetric effects on GNSS radio occultations: The ROHP–PAZ field campaign. *Atmos. Chem. Phys.* **16**: 635–649. https://doi.org/10.5194/acp-16-635-2016.

Padullés R, Cardellach E, Rius A. 2016b. Untangling rain structure from polarimetric GNSS radio occultation observables: A 2D tomographic approach. *Eur. J. Remote Sens.* **49**: 571–585. https://doi.org/10.5721/EuJRS20164930.

Phinney RA, Anderson DL. 1968. On the radio occultation method for studying planetary atmospheres. *J. Geophys. Res.* **73**: 1819–1827. https://doi.org/10.1029/JA073i005p01819.

Schiro KA, Neelin JD, Adams DK, Lintner BR. 2016. Deep convection and column water vapour over tropical land vs. tropical ocean: A comparison between the Amazon and the tropical western Pacific. *J. Atmos. Sci.* https://doi.org/10.1175/JAS-D-16-0119.1.

Seto S, Iguchi T. 2007. Rainfall-induced changes in actual surface backscattering cross sections and effects on rain-rate estimates by spaceborne precipitation radar. *J. Atmos. Oceanic Technol.* **24**: 1693–1709.

Skofronick-Jackson G, Petersen WA, Berg W, Kidd C, Stocker EF, Kirschbaum DB, Kakar R, Braun SA, Huffman GJ, Iguchi T, Kirstetter PE, Kummerow C, Meneghini R, Oki R, Olson WS, Takayabu YN, Furukawa K, Wilheit T. 2016. The Global Precipitation Measurement (GPM) mission for science and society. *Bull. Am. Meteorol. Soc.* https://doi.org/10.1175/BAMS-D-15-00306.1.

Spilker JJ, Axelrad P, Parkinson BW, Enge P. 1996. *Global Positioning System: Theory and Applications*, **I**. American Institute of Aeronautics and Astronautics. https://doi.org/10.2514/4.866388.

Susskind J, Barnet CD, Blaisdell JM. 2003. Retrieval of atmospheric and surface parameters from AIRS/AMSU/HSB data in the presence of clouds. *IEEE Trans. Geosci. Remote Sens.* **41**: 390–409.

Teunissen PJG, Montenbruck O. (eds.) 2017. *Springer: Handbook of Global Navigation Satellite Systems*. Springer International Publishing. https://doi.org/10.1007/978-3-319-42928-1.

Thébault E, Finlay CC, Beggan CD, Alken P, Aubert J, Barrois O, Bertrand F, Bondar T, Boness A, Brocco L, Canet E, Chambodut A, Chulliat A, Coisson P, Civet F, Du A, Fournier A, Fratter I, Gillet N, Hamilton B, Hamoudi M, Hulot G, Jager T, Korte M, Kuang W, Lalanne X, Langlais B, Léger J-M, Lesur V, Lowes FJ, Macmillan S, Mandea M, Manoj C, Maus S, Olsen N, Petrov V, Ridley V, Rother M, Sabaka TJ, Saturnino D, Schachtschneider R, Sirol O, Tangborn A, Thomson A, Toffner-Clausen L, Vigneron P, Wardinski I, Zvereva T. 2015. International geomagnetic reference field: The 12th generation. *Earth, Planets Space* **67**: 79. https://doi.org/10.1186/s40623-015-0228-9.

Vivekanandan J, Bringi VN, Hagen M, Meischner P. 1994. Polarimetric radar studies of atmospheric ice particles. *IEEE Trans. Geosci. Remote Sens.* **32**: 1–10.

Westra S, Fowler HJ, Evans JP, Alexander LV, Berg P, Johnson F, Kendon EJ, Lenderink G, Roberts NM. 2014. Future changes to the intensity and frequency of short-duration extreme rainfall. *Rev. Geophys.* **52**: 522–555.

Xie F, Haase JS, Syndergaard S. 2008. Profiling the atmosphere using the airborne GPS occultation technique: A sensitivity study. *IEEE Trans. Geosci. Remote Sens.* **46**(11): 3424–3435. https://doi.org/10.1109/TGRS.2008.2004713.